PAPER

Optical properties and limiting photocurrent of thin-film perovskite solar cells†

James M. Ball,‡[a] Samuel D. Stranks,§[a] Maximilian T. Hörantner,[a] Sven Hüttner,¶[b] Wei Zhang,[a] Edward J. W. Crossland,[c] Ivan Ramirez,[a] Moritz Riede,[a] Michael B. Johnston,[a] Richard H. Friend[b] and Henry J. Snaith*[a]

Metal-halide perovskite light-absorbers have risen to the forefront of photovoltaics research offering the potential to combine low-cost fabrication with high power-conversion efficiency. Much of the development has been driven by empirical optimisation strategies to fully exploit the favourable electronic properties of the absorber layer. To build on this progress, a full understanding of the device operation requires a thorough optical analysis of the device stack, providing a platform for maximising the power conversion efficiency through a precise determination of parasitic losses caused by coherence and absorption in the non-photoactive layers. Here we use an optical model based on the transfer-matrix formalism for analysis of perovskite-based planar heterojunction solar cells using experimentally determined complex refractive index data. We compare the modelled properties to experimentally determined data, and obtain good agreement, revealing that the internal quantum efficiency in the solar cells approaches 100%. The modelled and experimental dependence of the photocurrent on incidence angle exhibits only a weak variation, with very low reflectivity losses at all angles, highlighting the potential for useful power generation over a full daylight cycle.

Broader context

Over the last few years we have witnessed an unprecedented increase in the power conversion efficiency of solar cells based on solution processable organometal-halide perovskite light-absorbers, which now represent one of the most promising materials systems for future low-cost solar energy conversion. As these devices approach their achievable limits imposed by the electronic properties of their constituents, further advances will depend on the constraints imposed by their optical properties, which until now have received little attention. In thin-film stacks that comprise these solar cells, the light-coupling from the sun into the photoactive layer depends on internal reflections, coherence and parasitic absorption in a non-trivial manner. Additionally, for many real-world systems, the light-coupling must be maximised for a range of incidence angles over a daylight cycle imposing further design constraints. Here we provide the method and data to analyse these effects providing a deeper understanding of the device operation as well as a platform for future advances towards the absolute practical efficiency limits of perovskite-based photovoltaics.

Introduction

In the quest to develop alternative methods of energy production beyond fossil fuels, photovoltaic cells based on earth-abundant materials offer the possibility to supply a significant proportion of global energy demand sustainably with a reduced environmental impact. Among the myriad of semiconductor systems that have been proposed as solar cell light-absorbers, organic–inorganic halide perovskites have emerged as one of the most promising future competitors to silicon-based photovoltaics. This is enabled by the unique potential of this family of materials to satisfy the stringent requirements of coupling low embodied energy and low-cost production methods utilising earth-abundant raw materials with high power conversion efficiency.

A long-known subset of solution-processable hybrid organic–inorganic semiconducting perovskites[1] were first implemented

[a] *University of Oxford, Clarendon Laboratory, Parks Road, Oxford, OX1 3PU, UK. E-mail: h.snaith1@physics.ox.ac.uk*

[b] *University of Cambridge, Cavendish Laboratory, JJ Thomson Avenue, Cambridge, CB3 0HE, UK*

[c] *Oxford Photovoltaics, Begbroke Science Park, Begbroke Hill, Woodstock Road, Begbroke, Oxfordshire, OX5 1PF, UK*

‡ Current address: Istituto Italiano di Tecnologia, Center for Nanoscience and Technology, Via Pascoli 70/3, 20133 Milano, Italy.

§ Current address: Massachusetts Institute of Technology, 77 Massachusetts Avenue, Cambridge, MA, 02141, United States.

¶ Current address: Macromolecular Chemistry I, University of Bayreuth, Universitätstr. 30, 95447 Bayreuth, Germany.

in solar cells as discrete "sensitizer" nanoparticles in liquid-electrolyte photoelectrochemical devices,[2,3] with more recent solid-state analogues exhibiting impressive efficiency and stability enhancements.[4–7] Concurrently, developments in the understanding of the operational mechanism confirming long range charge-transport[4,8–10] following predominantly direct free-carrier generation,[11–14] has supported the use of conventional thin-film device architectures, simplifying the fabrication processes, which are typically solution-based at low-temperature.[15–19] Predominantly driven by improvements in materials processing, perovskite-based devices have reached certified power conversion efficiencies of over 20%,[20] which is unprecedented for photovoltaics over such a short development period.[16,21–25]

Among the challenges that lie ahead for further efficiency improvements, the analysis of the device structure as an optical stack is essential for optimising light-harvesting in the photo-active layer and maximising photocurrent generation. In real-world applications, the stack design must account for losses at all incidence angles due to the motion of the sun across the sky. In multijunction device architectures, the optical design has further significance where current matching of each junction whilst minimising parasitic losses is required to fully exploit efficiencies above the single-junction Shockley–Queisser limit.[26,27] For the complete analysis of the wavelength-dependence of the internal quantum efficiency (IQE), optical modelling is a reliable method that allows coherence effects and parasitic absorption to be accounted for in its derivation from the external quantum efficiency (EQE) spectra.[28–30] Fundamentally, the data required in the device model is also vital for spectroscopic measurements which aim to probe the photophysics of the absorber layer.

Here, we follow the transfer-matrix method to model a single-junction device stack using experimental complex refractive index data obtained from spectroscopic ellipsometry. The device configuration is shown in Fig. 1a in which we consider the most widely studied perovskite absorber to date, $CH_3NH_3PbI_3$ (Fig. 1b). The model is experimentally verified with device reflectance and transmission spectra. Based on the device spectral response, we use the model to derive the IQE spectrum accounting for coherence and parasitic absorption in a typical perovskite-based cell to reveal that up to 100% of all photons absorbed within the perovskite layer result in collected charge across the absorption region. Finally, we make use of the model to predict the dependence of the photocurrent on the incidence angle of the incident light and again realise good experimental agreement. The angular-dependence is an important indicator of the expected efficiency of a solar cell in real-world applications where the motion of the sun across the sky can influence current generation. We find that the perovskite-based solar cells, by virtue of the relatively low refractive index of $CH_3NH_3PbI_3$, would perform favourably in comparison to Si-based cells even without further optical optimisation with, for instance, anti-reflective coatings or surface structuring. All modelling data is included in the ESI† and the latest version of the code is freely available to download.[31]

Methods

Transfer-matrix optical modelling

When sunlight is incident upon a solar cell, the light's path through the device is determined by the wavelength-dependent complex refractive index, $\tilde{n} = \eta + i\kappa$, of each layer in the stack. η describes the phase velocity of light within the medium and κ is the dimensionless extinction coefficient accounting for attenuation of the optical electric field due to photoexcitation. In device architectures composed of thin-films (with thicknesses comparable to the wavelength of incident light), interference of the incident and reflected travelling waves from each interface will influence the optical electric-field distribution and therefore the position-dependent photoexcitation profile. Following light absorption, the photoexcited charge-carriers should be transported through the absorber to their corresponding carrier-selective contacts but must do so within a lifetime determined by the recombination mechanism within the absorber or at the interfaces. The photoexcitation profile is therefore a limiting factor for photocurrent generation, and is not only a property of the absorber but also of the other layers in the device stack.

To model the photoexcitation profile within a solar cell we utilise the generalised transfer-matrix method.[28,29,32–35] In the model the illumination source is located in air and the light is incident onto the cell through the glass substrate. The optical power density within each layer of the cell, represented by the Poynting vector, is calculated by first resolving the forward and backward propagating waves as the product of transfer matrices describing each interface. These matrices account for the fractional transmission and reflection at each interface and are determined by the s- and p- polarised Fresnel coefficients. The total optical power density at each point in the stack can then be calculated as the superposition of these waves within the coherent layers, allowing for light absorption. We make the
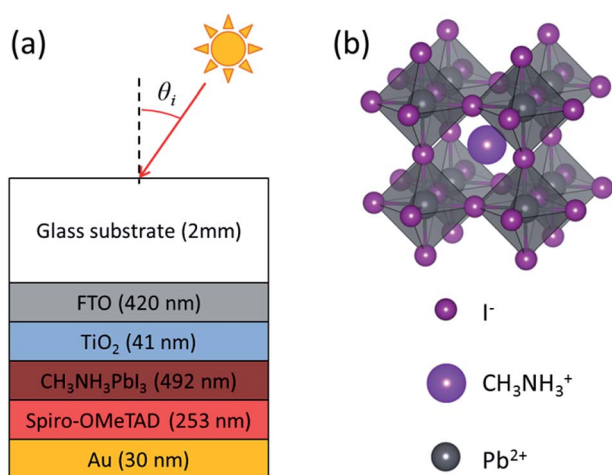

Fig. 1 (a) Device schematic of the p–i–n planar heterojunction configuration for a perovskite-based solar cell. (b) Crystal structure of the perovskite $CH_3NH_3PbI_3$.

This journal is © The Royal Society of Chemistry 2015

Energy Environ. Sci., 2015, **8**, 602–609 | **603**

approximation that superposition and absorption[36] can be neglected within the relatively thick air and glass layers which are thus treated as incoherent.[37] The carrier generation rate can then be derived from the power dissipated within the absorber. We allow the model to include all incidence angles to analyse the impact of the position of the sun on photovoltaic performance. We provide further details of the calculations in the ESI.† The latest version of our code is freely available to download.[31]

The input data for the model are the thickness and the experimentally derived complex refractive index spectra for each layer. For the present report, we have analysed the simple p–i–n planar heterojunction configuration as shown in Fig. 1a, although in principle the method and data could be used as a building block for the analysis of the many stack variations currently being explored in perovskite solar cells including mesoporous architectures, by employing an effective medium approximation. Our stack consists of a typical materials system for high-efficiency device performance: fluorine-doped tin oxide (FTO, TEC15) coated on glass serving as the substrate and transparent electrode connected to the external circuit; a compact layer of TiO_2 serving as the electron-selective layer; the perovskite absorber, $CH_3NH_3PbI_3$; 2,2′,7,7′-tetrakis-(*N*,*N*-di-4-methoxy-phenylamino)-9,9′-spirobifluorene (Spiro-OMeTAD) as the hole-selective layer; and a gold electrode connected to the external circuit.

Device fabrication

Devices were fabricated on glass substrates coated with fluorine-doped tin oxide (FTO, Pilkington TEC15, 12–14 Ω sq^{-1}). After etching the electrode pattern, the substrates were cleaned sequentially in hallmanex, deionised water, acetone, isopropanol and O_2 plasma. A compact layer of TiO_2 serving as the electron-selective contact was formed by spin coating a precursor solution (80 μl Ti–isopropoxide and 6 μl of 2 M HCl per ml of anhydrous ethanol) onto the FTO coated glass and heating it to 500 °C for 30 minutes. The substrates were then transferred to a nitrogen-filled glovebox where the perovskite film was prepared by spin coating a precursor solution of methylammonium iodide and lead acetate in dimethyl-formamide (DMF) in a 3 : 1 molar ratio followed by heating at 100 °C for 5 minutes. Further details of this process and characterisation will be published elsewhere.[38] The hole-transport material, 2,2′,7,7′-tetrakis-(*N*,*N*-di-4-methox-yphenylamino)-9,9′-spirobifluorene (Spiro-OMeTAD) was then spin-coated onto the perovskite from a 7 wt% solution in chlorobenzene containing 80 mol% lithium-bis(trifluoro-methane)sulfonimide and 30 mol% *tert*-butylpyridine as additives. Finally devices were completed by vacuum evaporation of 30 nm thick gold top contacts defined using a shadow mask.

Spectroscopic ellipsometry

Variable-angle (45–75°) spectroscopic ellipsometry was performed for each layer independently in a wavelength range from 300–900 nm. The films were prepared following the aforementioned procedures except using clean Si/SiO_2 wafers as the substrate. The measurements were performed using a J.A. Woolam Company ellipsometer, model M-2000DI, which is a rotating-compensator multichannel spectroscopic ellips-ometer. Modelling of the data was performed using VASE32 software by J.A. Woolam Company. The bare silicon oxide layer was measured, before the films were measured and resulted in a thickness of 306 nm. The films were measured by first determining their thickness using a Cauchy layer model in a range beyond their respective bandgap. Then the thickness was kept constant and a respective point-to-point fit was applied. For the perovskite layer a Kramers–Kronig consistent oscillator model was applied, resulting in much less noisy dielectric functions.

Device characterisation

For the completed solar cells the current–density as a function of voltage was measured using a Keithley 2400. Devices were illuminated under simulated AM 1.5 sunlight (ABET Sun 2000) with an effective irradiance of 104.7 mW cm^{-2} accounting for spectral mismatch (further details are included in the ESI†). The power of the lamp was calibrated using a KG5-filtered Si reference diode with NREL certification. The device area was defined with a shadow mask to be 0.0625 cm^2. Before measuring, devices were forward-biased at 1.4 V under illumination for 5 s. The voltage scan rate was 1 V s^{-1}.

For angle-dependent *J*–*V* measurements, the excitation source was a 532 nm CW laser (Suwtech LDC-800) with a spot size of ~0.1 cm^2. The intensity was set using optical density filters to give a density of photoexcitations equivalent to 1 sun illumination based on the equivalent photon flux. The angle was varied manually using a rotation stage.

The external quantum efficiency spectrum was measured by Fourier-transform photocurrent spectroscopy[39] using the solar cell as the detector in a Bruker Vertex Fourier-transform infrared spectrophotometer with a Xe lamp as the light source. The system was calibrated spectrally with an NREL certified Si reference diode. The absolute values were derived with a correction factor to provide the same integrated photocurrent as the device. Before measuring, devices were forward-biased at 1.4 V under illumination for 20 s. Further details of the method are provided in the ESI.†

$CH_3NH_3PbI_3$ and Spiro-OMeTAD layer thicknesses were estimated from scanning electron microscopy (Hitachi S-4300) images of devices in cross-section (error of ±13 nm). The gold thickness was estimated using a surface profilometer (Veeco Dektak 150) for an evaporated layer on a blank glass substrate (error ±1 nm). The TiO_2 and FTO thicknesses were estimated from spectroscopic ellipsometry.

Normal incidence transmission spectra were performed on complete devices using a PerkinElmer Lambda 1050 spectro-photometer. Reflectance spectra were obtained from complete devices at normal incidence using a Filmetrics F20-UV thin film analyser.

604 | *Energy Environ. Sci.*, 2015, **8**, 602–609

This journal is © The Royal Society of Chemistry 2015

Results and discussion

Spectroscopic ellipsometry

The primary data required for optical modelling of a device layer are careful measurements of the complex refractive index $\tilde{n}$ over the wavelength range of interest, *i.e.* where the absorption spectrum of the light-harvester overlaps with the solar spectrum. This is obtained by fitting the ellipsometric angles of the reflected polarisation state from the layer as a function of incidence angle and wavelength. With thickness and roughness as complementary data inputs, the complex refractive index can be extracted using a Kramers–Kronig consistent oscillator model to derive the pseudodielectric function from a previously obtained point-to-point fit for η and κ. We show the extracted η and κ spectra for the investigated perovskite in Fig. 2a based on a model of three Lorentz oscillators and one Tauc–Lorentz oscillator accounting for the predicted interband transitions and the band gap, respectively (further details are given in the ESI, section S1†).[40–43] The best fit to the data provided a bandgap energy of 1.56 eV which is in approximate agreement with alternative estimates.[40,41,44,45]

The peak value for the real part of the dielectric constant ($\mathcal{Re}[\varepsilon] = \eta^2 - \kappa^2$) of ~6.5 measured here for $CH_3NH_3PbI_3$ is in close agreement with a previous measurement of the dielectric constant at optical frequencies.[46] We show the full spectrum in Fig. 2b. The absorption coefficient for energies above the bandgap is also in good agreement with previous reports based on alternative techniques (shown in Fig. S4†).[30,47,48]

The extracted η and κ spectra for the other device layers are presented in the ESI, section S1.† The FTO coating on the glass substrate is itself a multilayer film of coherent layers whose optical properties are best reproduced with an additional roughness layer as an effective medium (see ESI Fig. S1†). In comparison to the values obtained for TiO_2 and Spiro-OMeTAD in this study, we observed small discrepancies between previous measurements[49] and our data (see ESI Fig. S3†), which is expected given the variation in deposition procedures. Complex refractive index data for noble metals has been reported previously in the literature, which we use in the subsequent device modelling.[50]

Optical modelling

The model not only predicts the optical electric-field within the cell but also the proportion of reflected and transmitted light. It therefore provides testable predictions that can be used to verify its validity *i.e.* the transmission and reflection spectra of the device stack. The model we used is based on the device stack shown in Fig. 1a, with the FTO coating as a multilayer stack (see Fig. S1a†), and two effective media at both FTO/TiO$_2$ (29 nm, ~65% volume fraction of FTO), and TiO$_2$/CH$_3$NH$_3$PbI$_3$ (41 nm, ~65% volume fraction of TiO$_2$) interfaces to account for surface roughness of the FTO and conformity of the electron selective layer.

In Fig. 3 we show the calculated and measured transmission and reflectance spectra for a standard device structure at normal light incidence. The measured reflectance loss of only ~5% for this device is comparable to typical AR-coated Si solar cells.[51–53] Notably the reflectivity of 5% is lower than the reflectivity of ~9% for an uncoated sheet of FTO glass, indicating that
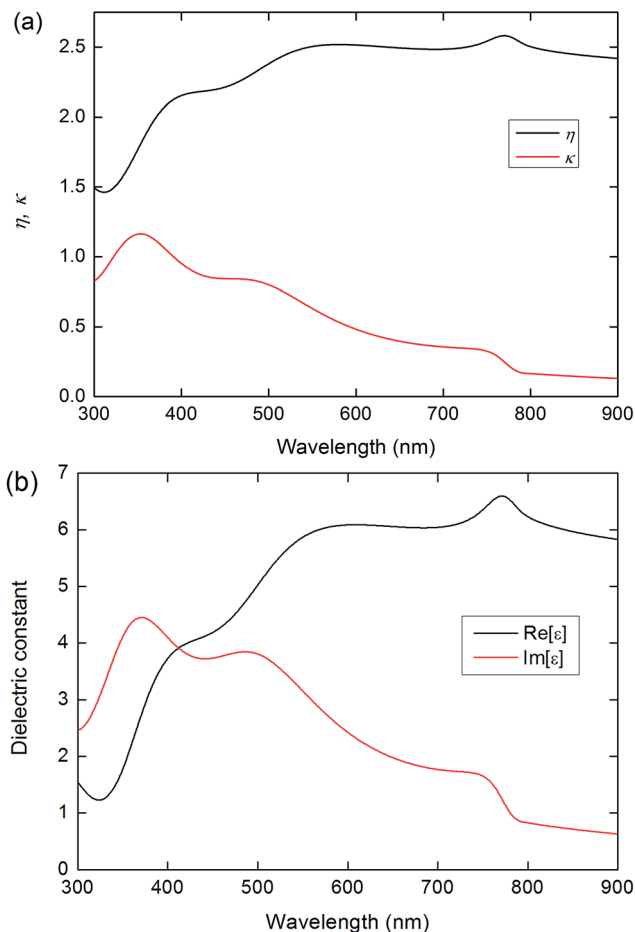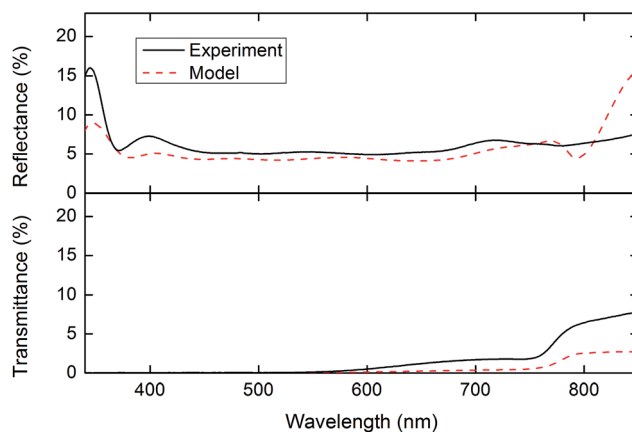

Fig. 2 The real and imaginary parts of the (a) complex refractive index and (b) dielectric constant extracted from the ellipsometry model and used in subsequent optical simulation of the device stack.

Fig. 3 Measured and calculated reflectance and transmittance spectra from a standard device using a 492 nm thick CH$_3$NH$_3$PbI$_3$ layer.

the multi-layer dielectric stack of the perovskite solar cell is already favourably set to minimise reflection losses. The model and experiment are in good agreement across the wavelength range where we expect photocurrent generation due to absorption of light with energies greater than the bandgap. Larger discrepancy occurs in the near infrared, possibly due to light leakage through pin holes in the thin gold contact. This will have only a small impact on the calculation of the light-harvesting efficiency at the band-edge. We present example predictions from the model such as the electric-field distribution and charge-generation profile in the ESI in Fig. S5.† For completeness, we present a comparison to finite-difference time-domain (FDTD) numerical simulations for the reflection and transmission spectra in ESI Fig. S7† exhibiting a similar level deviation from experiment.

Normal incidence solar cell measurements

To further compare the model with the real device performance we fabricated a planar heterojunction solar cell with the aforementioned device structure and measured it under simulated AM 1.5 sunlight (power density spectrum as shown in Fig. S6†), equivalent to 104.7 mW cm^{-2} irradiance (1.047 suns) over the absorption region of the perovskite. The experimental current–voltage characteristic for the device is given in Fig. S8,† generating a measured short-circuit current density, J_{sc}, of 22.6 mA cm^{-2}.

We measured the EQE for this device, as shown in Fig. 4a, using Fourier-transform photocurrent spectroscopy (FTPS).[39] The raw measurement provides the relative quantum efficiency which was scaled to give the equivalent integrated J_{sc} using the measured spectrum from the solar simulator (see ESI section S3.1†). The IQE spectrum, *i.e.* the wavelength dependence of the proportion of photoexcitons in CH$_3$NH$_3$PbI$_3$ that result in an electron–hole pair being extracted from the device, is derived from EQE = LHE × IQE, where LHE is the light-harvesting efficiency of the absorber layer, the proportion of incident light which is absorbed by the photoactive layer. The LHE is derived from the optical model accounting for coherence and parasitic absorption. We note here that measurements based on the reflection and absorption of the device and its constituents in an integrating sphere cannot adequately account for these effects and are therefore subject to greater uncertainty (see ESI section S3.4† for further discussion).[54]

We thus evaluate the IQE as a function of wavelength as we show in Fig. 4a. We find that the IQE is approximately 100% across a substantial proportion of the CH$_3$NH$_3$PbI$_3$ absorption spectrum, highlighting the efficient generation and collection of charge-carriers, which is essential for reaching the power conversion efficiency limit. This has been observed in other solution-processed photovoltaic systems but rarely with a commensurate flat and high LHE response across the absorption region.[55] Although the calculated IQE reaches a peak value of 101.7% at 600 nm, the extra current that would be generated from this "unphysical" excess is only ~0.3% of the total J_{sc} under the AM 1.5 spectrum, representing a small error. The main sources of uncertainty arise in the mismatch factor

calculation and J_{sc} measurement used to rescale the EQE, which are subject to lamp power instability (manufacturer specification is < ±3%). Uncertainty in the fitting of the raw ellipsometry data and thickness measurements also propagates through the transfer-matrix method leading to an error in the LHE (see ESI section S3.5† for further discussion).

Using our model based on the measured optical constants for each layer to account for optical losses in our device we find that for our measured thicknesses of the FTO glass, TiO$_2$, Spiro-OMeTAD, and the gold electrode, the photocurrent rises quickly with increasing perovskite thickness reaching ~20 mA cm^{-2} at 200 nm, and reaching close to its maximum value at 300 nm (see Fig. 4b) given the measured IQE spectrum in Fig. 4a. Thus, with the chosen contact materials, we observe nearly maximum light absorption for thicknesses above ~300 nm. Local maxima, highlighted with the dashed lines at ~190 nm, ~320 nm, ~470 nm and ~630 nm, in the thickness dependence arising from favourable interference conditions are weak in this system which relaxes the constraints for thicknesses uniformity within the range where the carrier-diffusion lengths are much longer than the film thickness. We note however that our estimated IQE drops off near the band edge, which may in part be due to the propagation in errors leading to low accuracy near the band edge. In the limit where the IQE is 100% across the measured spectrum then we expect that the photocurrent could continue to rise up to ~23–23.6 mA cm^{-2} for device relevant thicknesses in the range ~320–500 nm. Within this thickness range, near total light absorption is obtained in the perovskite layer leading to weak interference phenomena in the contact layers, as we show in ESI section S3.5.†

We have also used the model to estimate the optical losses, which are summarised in Fig. 4c in the wavelength range of 340–795 nm. For an active layer thickness of 492 nm, the parasitic losses due to light-absorption in the FTO multilayer, TiO$_2$, Spiro-OMeTAD, and gold electrode account for an equivalent of 1.72 mA cm^{-2} if it could all be converted into photocurrent. 1.38 mA cm^{-2} of this can be attributed to absorption in the FTO sub-layer as highlighted in Fig. 4d. Reflection at the incident interface between glass and air, light that is not absorbed after internal reflections, and light that is transmitted through the Au contact causes a loss of 1.36 mA cm^{-2}. This suggests that perhaps some of the biggest future performance enhancements from enhancing the absorption within the perovskite solar cells could come from the optical optimisation of the substrate materials and/or antireflective coatings. For a semiconductor with a bandgap of 1.56 eV (~795 nm) and a step-function absorption edge the maximum photocurrent which could be generated under 1 sun (AM 1.5, 100 mW cm^{-2}) illumination is 26.93 mA cm^{-2}. Light which we don't account for below 340 nm could generate an additional 0.25 mA cm^{-2} (an error of ~1% for these calculations), leaving an IQE loss of 2.16 mA cm^{-2} for the measured device. Hence for this material stack, with these reflective and parasitic absorption losses the maximum possible short-circuit photocurrent under AM 1.5 100 mW cm^{-2} sun light is 23.8 mA cm^{-2}, if a 100% IQE right across the visible spectrum can be achieved.
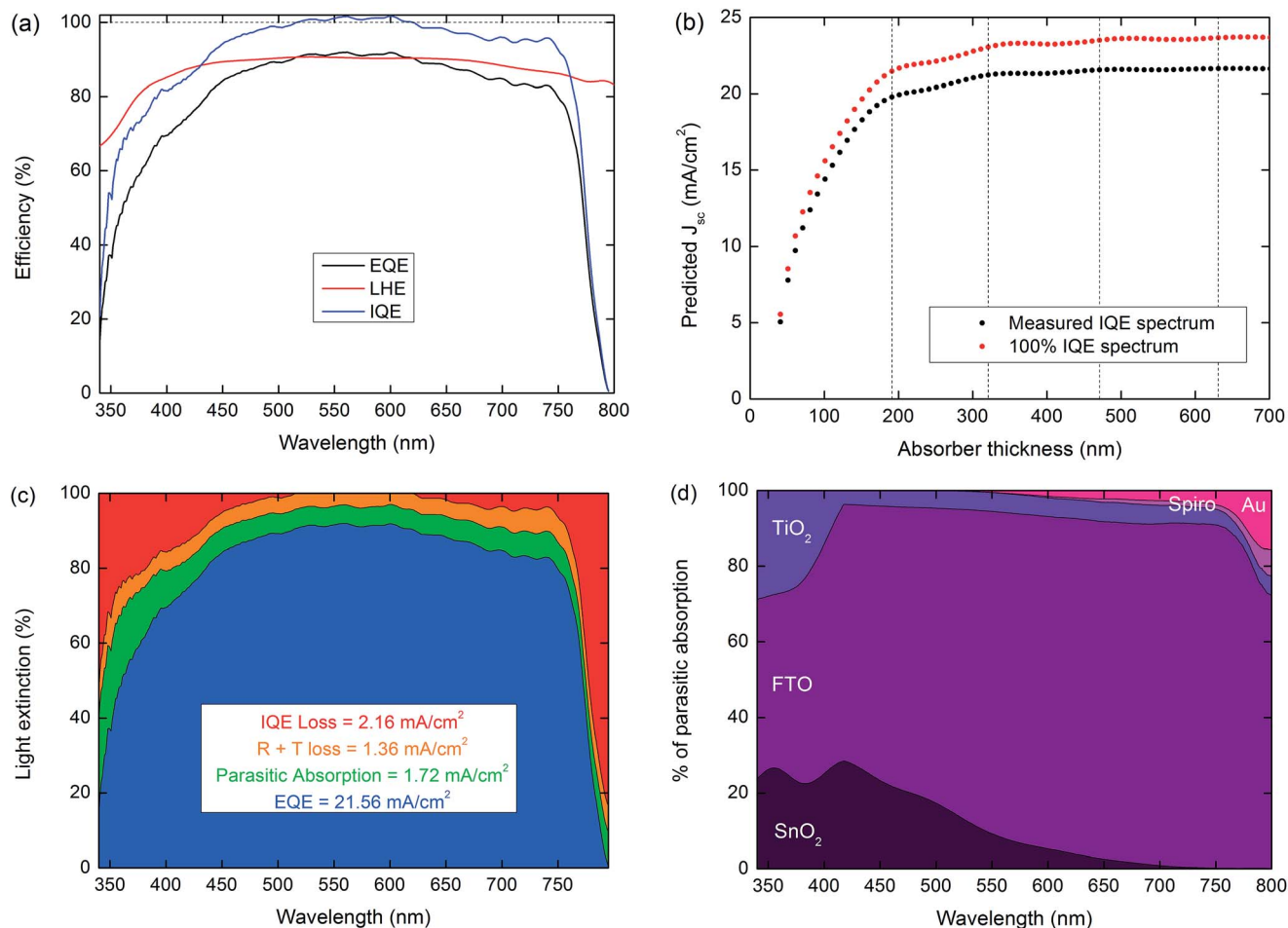
Fig. 4 (a) Measured EQE, calculated light–harvesting efficiency (LHE) from the transfer matrix model, and the derived IQE spectra. (b) Modelled dependence of the J_{sc} on $CH_3NH_3PbI_3$ thickness for the device structure shown in Fig. 1a assuming the derived IQE is constant with thickness (dashed lines highlight local maxima) in comparison to the assumption of 100% IQE across the spectrum. The absorber thickness includes the effective medium layer accounting for the roughness at the interface between TiO_2 and $CH_3NH_3PbI_3$. (c) Summary of light extinction highlighting the calculated losses when the solar cell is illuminated with the AM 1.5 spectrum. Calculations of current losses in IQE, parasitic absorption and reflection (R)/transmission (T) assume all light could be converted to current. (d) Breakdown of the proportion to total parasitic absorption losses within the non–active layers in the stack (TiO_2 accounts for the roughness layer as an effective medium of FTO and TiO_2). The glass substrate and SiO_2 layers contribute negligible absorption.

Angular dependent solar cell measurements

Finally, we have investigated the angular dependence of the incident illumination with the transfer-matrix model. To verify our model is able to accurately reproduce the variation of the cell performance at angles away from normal incidence, we collected experimental data using the setup illustrated in Fig. S11a.† We excite the sample with a TEM_{00} mode continuous-wave linearly polarised laser source at a wavelength of 532 nm, giving an approximately equivalent photoexcitation density to the 100 mW cm^{-2} AM 1.5 spectrum, and rotate the sample with respect to the source. These conditions can be accurately simulated with the model and Fig. S11b† again shows a good agreement with the experiment, including the absorption enhancement at the Brewster angle at the air/glass interface.

With confidence that the model accurately describes the solar cell incident angular dependence of J_{sc}, we proceeded to use it to predict the performance under the unpolarised AM 1.5

spectrum. Fig. 5 shows the incident angular dependence of the short-circuit current extracted from the model.

As the earth rotates throughout the day the incident angle, θ_i, of light onto the cell varies with respect to perpendicular illumination, the irradiance, and therefore J_{sc}, should decrease by a factor of cos θ_i corresponding to the scaling of the effective area of sunlight, assuming no spectral changes. Our data suggests a very weak angular dependence on incident illumination in comparison to the expected cos θ_i reduction in incident power density, similar to organic solar cells.[34] This is highly beneficial for solar cells in real-world applications where sun-tracking is currently impractical for non-concentrator based PV, and especially so for applications such as building integrated photovoltaics. Furthermore, in comparison, commercially available silicon modules require optical coatings to reduce severe reflection losses, that must be carefully designed to maintain their cos θ_i performance at oblique angles.[51–53] We

This journal is © The Royal Society of Chemistry 2015

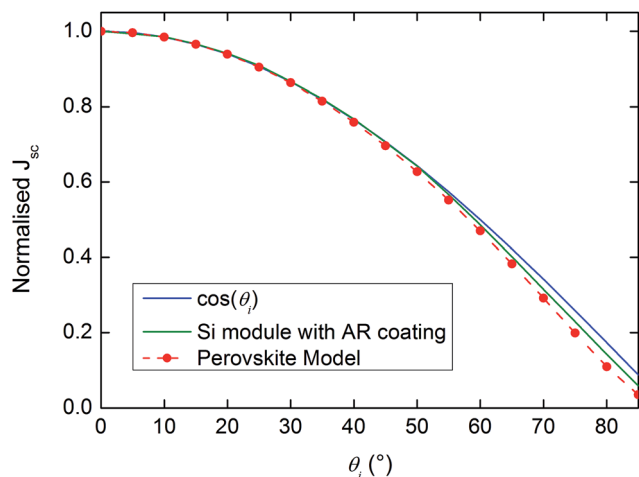*Energy Environ. Sci.*, 2015, **8**, 602–609 | 607

Fig. 5 Predicted angular dependence of the short-circuit current of a planar junction perovskite cell in comparison to literature data for a Si module with an antireflection layer, and the $\cos\theta_i$ function, which would be achieved for full absorption at all angles, accounting for reduced exposed area with tilt angle.[53]

also show in Fig. 5 some example experimental data from the literature for a commercial Si module with an antireflective coating. We find that even without optical engineering of the prototype laboratory perovskite device, the relatively low normal incidence reflectance loss is maintained over a wide angular range for perovskite-based solar cells, comparable to a commercial Si module. The favourable performance of these solar cells without additional coatings mainly arises from its relatively low refractive index compared to silicon, reducing the Fresnel reflection coefficients at the perovskite interfaces. This may further enhance the ability of perovskite solar cells to compete on cost with conventional technologies by potentially relaxing the requirements for additional layers and processing steps to obtain high performance throughout a daylight cycle. It may also be the case that the perovskite cell itself can effectively replace the anti-reflective coating on the silicon cell, when employed in a tandem configuration, serving two functions.

Conclusions

In summary we have successfully utilised a transfer-matrix optical model based on experimentally obtained optical constants for planar heterojunction perovskite solar cells. The model shows good agreement with both optical and electrical measurements leading to the extraction of the IQE spectrum accounting for coherence and parasitic absorption. This reveals that approximately 100% of absorbed photons in the perovskite layer result in collected charge across a broad range of its absorption spectrum. In addition we have found that these simple test devices exhibit high performance over a wide range of incidence angles suggesting that perovskite-based photovoltaics should provide useful power output in many configurations and deployments, including building integrated photovoltaics and under diffuse light. This work provides an additional platform for device optimisation towards further

increasing power conversion efficiencies as well as an important dataset for further photonic modelling and spectroscopic analysis of the fundamental properties of $CH_3NH_3PbI_3$.

Author contributions

The project was conceived, planned, and co-ordinated by JB and SS, supervised by HJS. MH wrote the code and performed simulations for the optical model with insight from IR (supervised by MR). SH performed VASE measurements and modelling to derive the optical constants, supervised by RF. WZ, JB and SS prepared materials for VASE and device measurements. JB, SS, MJ, and EC performed and analysed the device measurements. JB wrote the manuscript with contributions from all authors.

Acknowledgements

Notes and references

1 D. B. Mitzi, C. A. Feild, W. T. A. Harrison and A. M. Guloy, *Nature*, 1994, **369**, 467–469.
2 A. Kojima, K. Teshima, Y. Shirai and T. Miyasaka, *J. Am. Chem. Soc.*, 2009, **131**, 6050–6051.
3 J.-H. Im, C.-R. Lee, J.-W. Lee, S.-W. Park and N.-G. Park, *Nanoscale*, 2011, **3**, 4088.
4 M. M. Lee, J. Teuscher, T. Miyasaka, T. N. Murakami and H. J. Snaith, *Science*, 2012, **338**, 643–647.
5 H.-S. Kim, C.-R. Lee, J.-H. Im, K.-B. Lee, T. Moehl, A. Marchioro, S.-J. Moon, R. Humphry-Baker, J.-H. Yum, J. E. Moser, M. Grätzel and N.-G. Park, *Sci. Rep.*, 2012, **2**, 591.
6 J. H. Noh, S. H. Im, J. H. Heo, T. N. Mandal and S. Il Seok, *Nano Lett.*, 2013, **13**, 1764–1769.
7 N. J. Jeon, J. H. Noh, Y. C. Kim, W. S. Yang, S. Ryu and S. Il Seok, *Nat. Mater.*, 2014, 1–7.
8 S. D. Stranks, G. E. Eperon, G. Grancini, C. Menelaou, M. J. P. Alcocer, T. Leijtens, L. M. Herz, A. Petrozza and H. J. Snaith, *Science*, 2013, **342**, 341–344.
9 E. Edri, S. Kirmayer, S. Mukhopadhyay, K. Gartsman, G. Hodes and D. Cahen, *Nat. Commun.*, 2014, **5**, 3461.
10 C. Wehrenfennig, G. E. Eperon, M. B. Johnston, H. J. Snaith and L. M. Herz, *Adv. Mater.*, 2014, **26**, 1584–1589.
11 V. D'Innocenzo, G. Grancini, M. J. P. Alcocer, A. R. S. Kandada, S. D. Stranks, M. M. Lee, G. Lanzani, H. J. Snaith and A. Petrozza, *Nat. Commun.*, 2014, **5**, 3586.
12 F. Deschler, M. Price, S. Pathak, L. E. Klintberg, D. D. Jarausch, R. Higler, S. Hüttner, T. Leijtens, S. D. Stranks, H. J. Snaith, M. Atatüre, R. T. Phillips and R. H. Friend, *J. Phys. Chem. Lett.*, 2014, **5**, 1421–1426.
13 J. S. Manser and P. V. Kamat, *Nat. Photonics*, 2014, **8**, 737–743.

14 S. D. Stranks, V. M. Burlakov, T. Leijtens, J. M. Ball, A. Goriely and H. J. Snaith, *Phys. Rev. Applied 2*, 2014, 034007.

15 J. M. Ball, M. M. Lee, A. Hey and H. J. Snaith, *Energy Environ. Sci.*, 2013, **6**, 1739–1743.

16 P. Docampo, J. M. Ball, M. Darwich, G. E. Eperon and H. J. Snaith, *Nat. Commun.*, 2013, **4**, 2761.

17 G. E. Eperon, V. M. Burlakov, P. Docampo, A. Goriely and H. J. Snaith, *Adv. Funct. Mater.*, 2014, **24**, 151–157.

18 M. Liu, M. B. Johnston and H. J. Snaith, *Nature*, 2013, **501**, 395–398.

19 Q. Chen, H. Zhou, Z. Hong, S. Luo, H.-S. Duan, H.-H. Wang, Y. Liu, G. Li and Y. Yang, *J. Am. Chem. Soc.*, 2014, **136**, 622–625.

20 NREL, http://www.nrel.gov/ncpv/images/efficiency_chart.jpg, accessed 10th October 2014.

21 J. T.-W. Wang, J. M. Ball, E. M. Barea, A. Abate, J. a. Alexander-Webber, J. Huang, M. Saliba, I. Mora-Sero, J. Bisquert, H. J. Snaith and R. J. Nicholas, *Nano Lett.*, 2014, **14**, 724–730.

22 K. Wojciechowski, M. Saliba, T. Leijtens, A. Abate and H. J. Snaith, *Energy Environ. Sci.*, 2014, **7**, 1142–1147.

23 M. H. Kumar, N. Yantara, S. Dharani, M. Graetzel, S. Mhaisalkar, P. P. Boix and N. Mathews, *Chem. Commun.*, 2013, **49**, 11089–11091.

24 D. Liu and T. L. Kelly, *Nat. Photonics*, 2014, **8**, 133–138.

25 H. Zhou, Q. Chen, G. Li, S. Luo, T.-b. Song, H.-S. Duan, Z. Hong, J. You, Y. Liu and Y. Yang, *Science*, 2014, **345**, 542–546.

26 W. Shockley and H. J. Queisser, *J. Appl. Phys.*, 1961, **32**, 510.

27 Z. M. Beiley and M. D. McGehee, *Energy Environ. Sci.*, 2012, **5**, 9173.

28 L. A. A. Pettersson, L. S. Roman and O. Inganas, *J. Appl. Phys.*, 1999, **86**, 487–496.

29 G. F. Burkhard, E. T. Hoke and M. D. McGehee, *Adv. Mater.*, 2010, **22**, 3293–3297.

30 S. Sun, T. Salim, N. Mathews, M. Duchamp, C. Boothroyd, G. Xing, T. C. Sum and Y. M. Lam, *Energy Environ. Sci.*, 2014, **7**, 399–407.

31 https://github.com/matoho/tmm_solarcell.

32 M. Young, C. J. Traverse, R. Pandey, M. C. Barr and R. R. Lunt, *Appl. Phys. Lett.*, 2013, **103**, 133304.

33 E. Centurioni, *Appl. Opt.*, 2005, **44**, 7532–7539.

34 D. Cheyns, B. P. Rand, B. Verreet, J. Genoe, J. Poortmans and P. Heremans, *Appl. Phys. Lett.*, 2008, **92**, 243310.

35 S. Byrnes, http://sjbyrnes.com/?page_id=12, accessed 22nd September 2014.

36 M. Rubin, *Sol. Energy Mater.*, 1985, **12**, 275–288.

37 K. Kang, S. Lee and J. Kim, *Jpn. J. Appl. Phys.*, 2013, **52**, 052301.

38 W. Zhang, *et al. Ultra-smooth organic–inorganic perovskite thin-film formation and crystallization for Efficient Planar Heterojunction Solar Cells*, submitted, 2014.

39 M. Vanecek and A. Poruba, *Appl. Phys. Lett.*, 2002, **80**, 719–721.

40 P. Umari, E. Mosconi and F. De Angelis, *Sci. Rep.*, 2014, **4**, 4467.

41 J. Even, L. Pedesseau and C. Katan, *J. Phys. Chem. C*, 2014, **118**, 11566–11572.

42 H. G. Tompkins, *Handbook of Ellipsometry*, 2005, vol. 30.

43 G. N. Maracas, C. H. Kuo, S. Anand and R. Droopad, *J. Appl. Phys.*, 1995, **77**, 1701–1704.

44 C. C. Stoumpos, C. D. Malliakas and M. G. Kanatzidis, *Inorg. Chem.*, 2013, **52**, 9019–9038.

45 T. Baikie, Y. Fang, J. M. Kadro, M. Schreyer, F. Wei, S. G. Mhaisalkar, M. Graetzel and T. J. White, *J. Mater. Chem. A*, 2013, **1**, 5628.

46 M. Hirasawa, T. Ishihara, T. Goto, K. Uchida and N. Miura, *Phys. Rev. B: Condens. Matter Mater. Phys.*, 1994, **201**, 427–430.

47 S. De Wolf, J. Holovsky, S. J. Moon, P. Löper, B. Niesen, M. Ledinsky, F. J. Haug, J. H. Yum and C. Ballif, *J. Phys. Chem. Lett.*, 2014, **5**, 1035–1039.

48 G. Xing, N. Mathews, S. Sun, S. S. Lim, Y. M. Lam, M. Grätzel, S. Mhaisalkar and T. C. Sum, *Science*, 2013, **342**, 344–347.

49 A. J. Moule, H. J. Snaith, M. Kaiser, H. Klesper, D. M. Huang, M. Gratzel and K. Meerholz, *J. Appl. Phys.*, 2009, **106**, 073111.

50 P. B. Johnson and R. W. Christy, *Phys. Rev. B: Condens. Matter Mater. Phys.*, 1972, **6**, 4370–4379.

51 H. K. Raut, V. A. Ganesh, A. S. Nair and S. Ramakrishna, *Energy Environ. Sci.*, 2011, **4**, 3779.

52 M.-L. Kuo, D. J. Poxson, Y. S. Kim, F. W. Mont, J. K. Kim, E. F. Schubert and S.-Y. Lin, *Opt. Lett.*, 2008, **33**, 2527–2529.

53 J. L. Balenzategui and F. Chenlo, *Sol. Energy Mater. Sol. Cells*, 2005, **86**, 53–83.

54 J. M. Ball, M. M. Lee, A. Hey and H. J. Snaith, *Energy Environ. Sci.*, 2013, **6**, 1739–1743.

55 S. H. Park, A. Roy, S. Beaupré, S. Cho, N. Coates, J. S. Moon, D. Moses, M. Leclerc, K. Lee and A. J. Heeger, *Nat. Photonics*, 2009, **3**, 297–302.